

# Separating Double-Beta Decay Events from Background in a Kiloton-Scale Directional Liquid Scintillator Detector

Andrey Elagin<sup>a,\*</sup>, Henry J. Frisch<sup>a</sup>, Jonathan Ouellet<sup>b</sup>, Lindley Winslow<sup>b</sup>, **Opt in**<sup>c</sup>

<sup>a</sup> *Enrico Fermi Institute, University of Chicago, Chicago, IL, 60637*

<sup>b</sup> *Massachusetts Institute of Technology, Cambridge, MA 02139*

<sup>c</sup> **Please opt-in if you think you should be on the author list**

---

## Abstract

We propose a technique for separating  $0\nu\beta\beta$ -decay events from background due to  $^{10}\text{C}$  decays and  $^8\text{B}$  solar neutrino interactions in a liquid scintillator detector. These represent the key backgrounds at shallow and deep sites. The technique compares event topology of the signal and background events using spherical harmonics analysis of the early light emitted in  $0\nu\beta\beta$ -decay and  $^8\text{B}$  events. Selection of early photons using fast photo-detectors allows for separation of directional Cherenkov from isotropic scintillation light and identification of two event topologies based on the spatial distribution of the early photons in the detector.

---

---

\*Corresponding Author: elagin@hep.uchicago.edu

8 **Contents**

9	<b>1 Introduction</b>	<b>3</b>
10	<b>2 Detector Model</b>	<b>5</b>
11	<b>3 Event Topology and Spherical Harmonics Analysis</b>	<b>9</b>
12	3.1 Topology of $0\nu\beta\beta$ -decay and ${}^8B$ Events . . . . .	9
13	3.2 Description of Spherical Harmonics Analysis . . . . .	10
14	3.3 Spherical Harmonics Analysis and Off-center Events . . . . .	13
15	3.4 Implementation of the spherical harmonics analysis . . . . .	13
16	<b>4 Performance and Experimental Challenges</b>	<b>17</b>
17	4.1 Performance of the spherical harmonics analysis on $0\nu\beta\beta$ decay and ${}^8B$ events. . . . .	17
18	4.2 Experimental challenges . . . . .	18
19	<b>5 Conclusions</b>	<b>23</b>
20	<b>A <math>0\nu\beta\beta</math> decay vs <math>{}^{10}C</math> background</b>	<b>24</b>

## 1. Introduction

Over the past decade, neutrino oscillation experiments have conclusively established that neutrinos have mass. However, one of the most fundamental and still open questions in particle physics is the nature of that mass. Is the neutrino unique in the Standard Model with a Majorana type mass, as is predicted by most theoretical arguments, or does it have a Dirac type mass, like the rest of the fermions in the Standard Model? A Majorana mass would have far reaching implications, from explaining the lightness of the neutrino and providing a bridge to higher energy phenomena through the see-saw mechanism [CITATION] to providing the required lepton-number violation (LNV) and CP-violation needed for leptogenesis to explain the baryon asymmetry of the universe [1]. Conversely, a Dirac neutrino could point to an underlying symmetry of the Universe. Presently, the most promising technique for answering these questions is the search for Neutrinoless Double-Beta ( $0\nu\beta\beta$ ) decay [CITATION]. In this decay, a nucleus undergoes a second order  $\beta$ -decay without producing any neutrinos,  $(Z, A) \rightarrow (Z + 2, A) + 2\beta^-$ . The resulting decay products are ejected with a total kinetic energy equal to the decay  $Q$ -value, and most of this is carried by the electrons which have typical kinetic energies of  $\sim 1\text{--}2$  MeV.

The standard mechanism of  $0\nu\beta\beta$  decay is parameterized by the *effective Majorana mass*,  $m_{\beta\beta} \equiv \left| \sum_i U_{ei}^2 m_i \right|$ , where  $U_{ei}$  are the elements of the PMNS matrix and  $m_i$  are the neutrino masses [CITATION]. Recently, this search has generated a significant amount of experimental interest, with current experiments searching for  $0\nu\beta\beta$  decay of  $^{76}\text{Ge}$  [2],  $^{130}\text{Te}$  [3] and  $^{136}\text{Xe}$  [4, 5]. At present,  $0\nu\beta\beta$  decay has never been convincingly observed, but limits place the half-lives at longer than  $10^{23}\text{--}10^{25}$  yr in the isotopes studied. These limits translate to a limit on  $m_{\beta\beta} \lesssim 150\text{--}700$  meV, with the majority of the spread on this limit coming from uncertainty in the nuclear modeling. The next generation of  $0\nu\beta\beta$  decay experiments seek to be sensitive enough to detect or rule out  $0\nu\beta\beta$  decay down to  $m_{\beta\beta} < 10$  meV. This will require, among other things,  $\sim$ a ton of active isotope, a good energy resolution, and a near zero background in the region of interest (ROI) [CITATION?].

Over the past few years, liquid scintillator-based detectors have proven to be a competitive technology in this search [CITATION?]. Their primary advantage is in their scalability to larger active masses, which entails dissolving larger amounts of active isotope into the liquid scintillator (LS). This feature allows for rapid scaling to the 1 ton or more of active isotope. In a large LS detector, where backgrounds from the outside of the detector can be efficiently self-shielded or tagged and vetoed, the two backgrounds relevant to  $0\nu\beta\beta$  decay are  $2\nu\beta\beta$  and electron scattering (ES) interactions of  $^8\text{B}$  solar neutrinos.

Two neutrino double beta ( $2\nu\beta\beta$ ) decay is the Standard Model allowed second order  $\beta$ -decay channel where lepton number is conserved,  $(Z, A) \rightarrow (Z, A + 2) + 2\beta + 2\bar{\nu}_e$ . Since the kinetic energy of the neutrinos is practically never detected, the resulting  $2\nu\beta\beta$  spectrum is broadened from 0 MeV up to the decay  $Q$ -value. The high energy tail of this spectrum forms a background for the  $0\nu\beta\beta$  signal. Since it is intrinsic to the target isotope and the decay kinematics are nearly identical to  $0\nu\beta\beta$  decay,  $2\nu\beta\beta$  can only be separated from  $0\nu\beta\beta$  with a detector with powerful enough resolution (see Fig. 1). Present LS-based detectors achieve typical energy resolutions of  $\sigma(E) \sim 5\% / \sqrt{E(\text{MeV})}$ . The next

generation of detectors will improve up this... Something about photo-coverage (etc). Eventually this will fold back in the question of slowing down the scintillation signal and improving the Cherenkov signal at the cost of decreasing the total light yield.

The spectrum of ES interactions of  $^8\text{B}$  solar neutrinos falls slowly over the range 2–3 MeV, creating a nearly flat background across the  $0\nu\beta\beta$  ROI. However, these interactions produce only a single  $\sim 2.5$  MeV electron, rather than two  $\sim 1.2$  MeV electrons as in  $0\nu\beta\beta$ . In a LS, this difference in event topology manifests as two distinct distributions of Cherenkov photons, and thus creates a way to tag and remove these  $^8\text{B}$  solar neutrino events. As we have shown in previous works, photo-detectors with timing resolution of  $\sim 100$  ps can resolve the prompt Cherenkov photons from the slower scintillation signal [6]. The challenge is that for a given event, we expect XXX Cherenkov photons with which to reconstruct the event topology.

In this paper, we proposed to use a spherical harmonic decomposition to analyze the distribution of early photo-electrons (PE) to discriminate between  $^8\text{B}$  solar neutrinos and  $0\nu\beta\beta$  decay events. In Section 2, we describe the detector model we will use throughout this paper. In Section ??, we introduce the spherical harmonic decomposition, and discuss the performance of this analysis in Section 4.

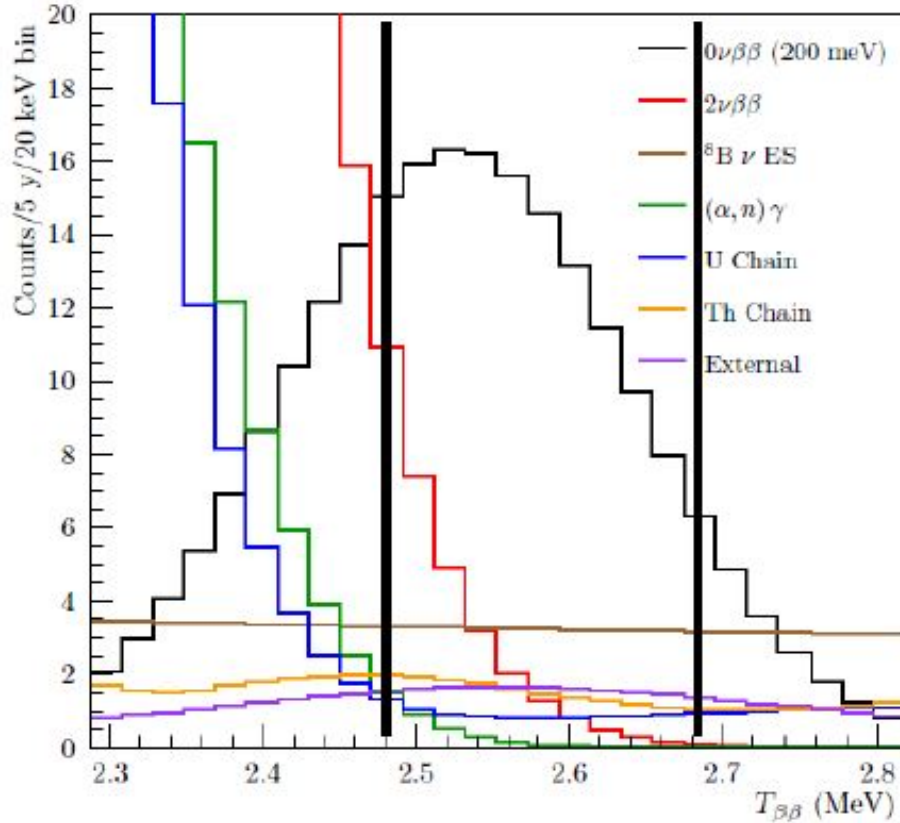


Figure 1: SNO+ Phase I signal and background energy spectrum (visible kinetic energy reconstructed under a  $0\nu\beta\beta$  hypothesis). Plot taken from [?]

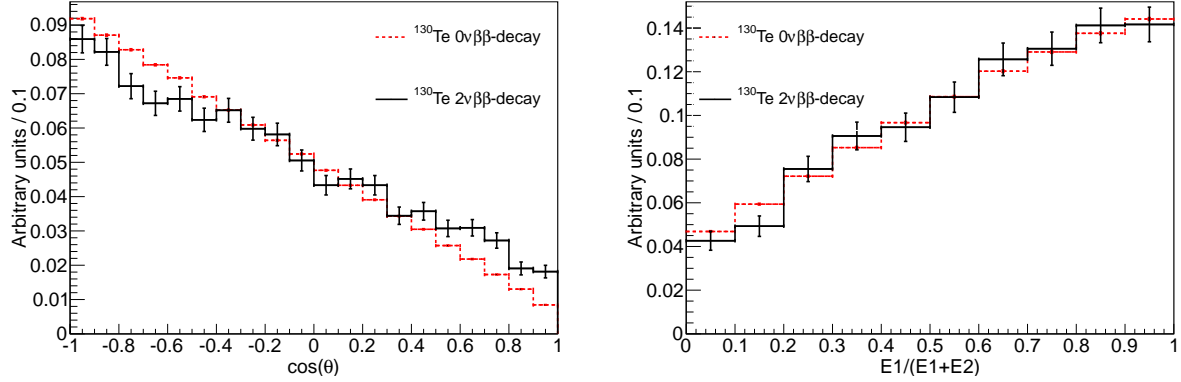


Figure 2: Comparison between kinematics of  $0\nu\beta\beta$  (dashed red lines) and  $2\nu\beta\beta$  decays (solid black lines) for events with the total kinetic energy of the electrons above 90% of the Q-value. *Left:* Cosine of the angle between two electrons. *Right:* Fraction of energy carried by one of the two electrons. Due to limited statistic around the energy spectrum end point for  $2\nu\beta\beta$  decay we show statistical errors for each bin.

## 2. Detector Model

In order to study the topology of  $0\nu\beta\beta$  decay and background events in a liquid scintillator detector, a Geant4[7, 8] simulation has been constructed. This is the same simulation used in our preceding paper [6]. Therefore, we limit out discussion of the simulation to a summary of the the most relevant simulation parameters.

The simulation uses Geant4 version 4.9.6. We use the default liquid scintillator optical model, in which optical photons are assigned the group velocity in the wavelength region of normal dispersion.

The detector geometry is a sphere of 6.5 m radius filled with scintillator. The default scintillator composition has been chosen to match a KamLAND-like scintillator[9]: 80% n-dodecane, 20% pseudocumene and 1.52 g/l PPO. The scintillator properties implemented in the simulation include

- the atomic composition and density ( $\rho = 0.78$  g/ml),
- the wavelength-dependent attenuation length[10] and refractive index[11],
- the scintillation emission spectrum[10],
- emission rise time ( $\tau_r = 1.0$  ns) and emission decay time constants ( $\tau_{d1} = 6.9$  ns and  $\tau_{d2} = 8.8$  ns with relative weights of 0.87 and 0.13)[12],
- scintillator light yield (9030 photons/MeV), and
- the Birks constant ( $k_B \approx 0.1$  mm/MeV)[13].

The attenuation length at 400 nm, which is the position of the peak standard bialkali photocathode efficiency, is 25 m. The attenuation length drops precipitously from 6.5 m to 0.65 m between 370 nm and 360 nm. We use this drop to define the cutoff wavelength at 370 nm. This is a standard scintillator. However, we do deviate from the baseline

KamLAND case in that the re-emission of absorbed photons in the scintillator bulk volume and optical scattering, specifically Rayleigh scattering, has not yet been included. A test simulation shows that the effect of optical scattering is negligible [6].

The inner sphere surface is used as the photodetector. It is treated as fully absorbing (no reflections), with a photodetector coverage of 100%. As in the case of optical scattering, reflections at the sphere are a small effect that would create a small tail at longer times. The default is the QE of a bialkali photocathode (Hamamatsu R7081 PMT)[14]. The QE values as a function of wavelength come from the Double Chooz[15] Monte Carlo simulation. We note that the KamLAND 17-inch PMTs use the same photocathode type with similar quantum efficiency. We are neglecting any threshold effects in the photodetector readout electronics.

Four effects primarily contribute to the timing of the scintillator detector system: the travel time of the particle, the time constants of the scintillation process, chromatic dispersion, and the timing of the photodetector.

In the energy range important for  $0\nu\beta\beta$ , a 1.4 MeV electron travels a total path length of 0.8 cm, has a distance from the origin of 0.6 cm in  $0.030\pm0.004$  ns and takes  $0.028\pm0.004$  ns to drop below Cherenkov threshold. We note that due to scattering of the electron, the final direction of the electron before it stops does not correspond to the initial direction; however the scattering angle is small while the majority of Cherenkov light is produced. The Cherenkov light thus still encodes the direction of the primary electron. The scattering physics is handled by Geant4's "Multiple Scattering" process which is valid down to 1 keV, where atomic shell structure becomes important[16].

The scintillator-specific rise and decay times are the second effect that determines the timing in a scintillator detector. The first step in the scintillation process is the transfer of energy from the solvent to the solute. The time constant of this energy transfer accounts for a rise time in scintillation light emission. Because past neutrino experiments were not highly sensitive to the effect of the scintillation rise time, there is a lack of accurate measurements of this property. We assume a rise time of 1.0 ns – but more detailed studies are needed in the future. The two time constants used to describe the falling edge of the scintillator emission time distribution (quoted above) are values specific to the KamLAND scintillator.

Chromatic dispersion is the third effect that determines the timing in a scintillator detector. Due to the wavelength-dependence of the refractive index the speed of light in the scintillator increases with increasing photon wavelengths for normal dispersion, with red light traveling faster than blue light.

Photoelectrons coming from Cherenkov light are on average created about 0.5 ns earlier than PE's from scintillation light. The RMS values from PE time distributions for Cherenkov and scintillation light are both about 0.5 ns. Note that these numbers include the effect of the finite electron travel time.

The fourth effect determining the timing in a scintillator detector is the timing of the photodetectors. The measurement of the arrival times of single photoelectrons is affected by the transit-time spread (TTS) of the photodetectors, a number which can be different by orders of magnitude depending on the detector type. We use a TTS of 0.1 ns ( $\sigma$ ), which can be achieved with large area picosecond photodetectors (LAPPDs)[17–24].

The primary quantities provided by the Geant4 simulation are the photoelectron hit positions and the detection

times after the TTS resolution has been applied. These quantities are then used for event topology reconstruction.

Figures 3 and 4 show the output of the detector simulation discussed in this section. Left panel in Fig. 3 compares PE arrival time between Cherenkov and scintillation light for 1000 simulated  $^{130}\text{Te}$   $0\nu\beta\beta$ -decay events. The right panel in Fig. 3 compares the Cherenkov PE arrival times between  $^{130}\text{Te}$   $0\nu\beta\beta$ -decay and  $^8\text{B}$  events.  $^8\text{B}$  events produce a slightly higher number of the Cherenkov photons because they have only one electron carrying the same kinetic energy as opposed to the two electrons in the case of  $0\nu\beta\beta$ -decay events. Distributions of the scintillation PEs' arrival time are indistinguishable between  $^{130}\text{Te}$   $0\nu\beta\beta$  decay and  $^8\text{B}$  due to identical total energy in the event,  $Q(^{130}\text{Te}) = 2.526$  MeV.

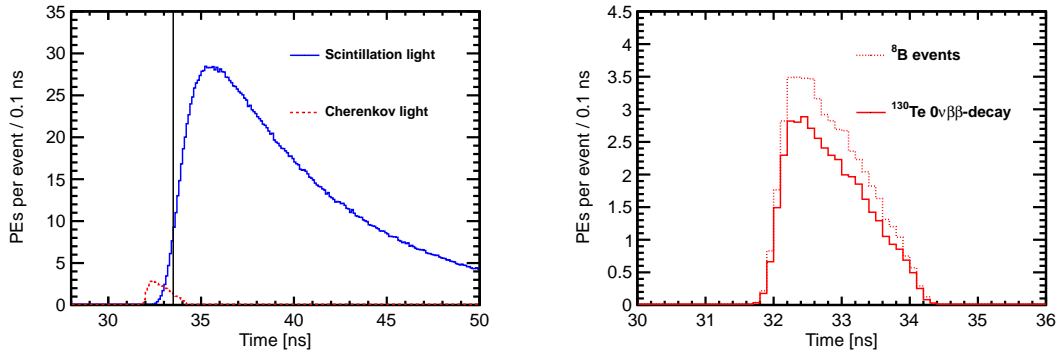


Figure 3: *Left*: Photo-electron (PE) arrival times after application of the photo-detector transit time spread (TTS) of 100 ps for the simulation of 1000  $0\nu\beta\beta$  decay events of  $^{130}\text{Te}$  at the center of the detector. PEs from Cherenkov light (*dashed red line*) and scintillation light (*solid blue line*) are compared. The black vertical line illustrates a time cut at 33.5 ns. *Right*: Comparison between Cherenkov PEs arrival time for  $^{130}\text{Te}$   $0\nu\beta\beta$  decay (*solid line*) and  $^8\text{B}$  (*dotted line*) events. **Distributions of the scintillation PEs arrival time are indistinguishable between  $^{130}\text{Te}$   $0\nu\beta\beta$  decay and  $^8\text{B}$  due to identical total energy in the event,  $Q(^{130}\text{Te}) = 2.526$  MeV.**

As shown in Fig. 3, a time cut of 33.5 ns on the PE arrival time selects a sample of early PEs that includes the majority of Cherenkov photons. Scintillation PEs also are selected with this time cut. Figure 4 shows the total number of scintillation and Cherenkov PE per event for  $0\nu\beta\beta$  signal and  $^8\text{B}$  background events. The  $^8\text{B}$  events do have a higher number of Cherenkov PEs on average compared to  $0\nu\beta\beta$  events because of the single electron in  $^8\text{B}$  events has a higher energy than the two electrons from  $0\nu\beta\beta$  decay. This difference, though, is not significant enough to be used alone as a reliable discriminant between  $0\nu\beta\beta$ -decay and  $^8\text{B}$  events. However, it may provide an extra handle on signal-background separation in combination (e.g. by using multivariate techniques) with other event parameters.

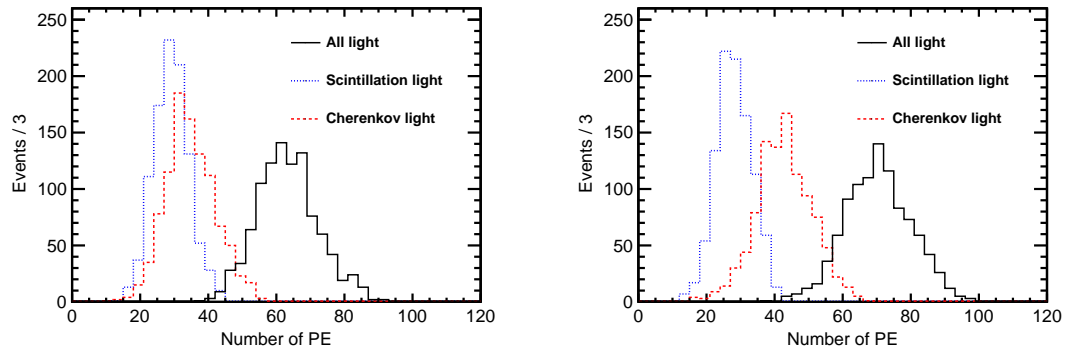


Figure 4: Number of Cherenkov (*dashed red line*), scintillation (*dotted blue line*), and total (*solid black line*) PEs for the simulation of 1000  $^{130}\text{Te}$   $0\nu\beta\beta$  decay (left panel) and  $^8\text{B}$  (right panel) events.



### 3. Event Topology and Spherical Harmonics Analysis

#### 3.1. Topology of $0\nu\beta\beta$ -decay and ${}^8B$ Events

For all isotopes considered for searches of  $0\nu\beta\beta$ -decay, the electrons emitted by the process with energies around the Q-value will be above Cherenkov threshold in liquid scintillators. Each electron above the threshold will produce a fuzzy ring of Cherenkov light at the detector surface. The fuzziness of the ring depends on electron scattering. In most cases Cherenkov rings from low energy electrons degrade to randomly shaped clusters of Cherenkov photons around the direction of the electron track.

A large fraction of  $0\nu\beta\beta$ -decay events will have two Cherenkov clusters<sup>1</sup> as opposed to one cluster from  ${}^8B$  events. Therefore, accurately distinguishing between a  $0\nu\beta\beta$ -decay signal from a  ${}^8B$  background event depends on the ability to identify the topology of Cherenkov light on the detector sphere on top of uniformly distributed scintillation light. We show that an analysis of spherical harmonics on the spatial distribution of early photons can be used to separate  $0\nu\beta\beta$ -decay and from  ${}^8B$  events.

In order to illustrate differences between different event topologies, we introduce three example event topologies: two electrons produced back-to-back at an  $180^\circ$  angle, two electrons at a  $90^\circ$  angle, and a single electron. The first two are representative of topologies for  $0\nu\beta\beta$ -decay signal events while the latter is representative of  ${}^8B$  background events. Figure 5 shows the Cherenkov photon distributions of 5 MeV electrons for each of the three topologies. Each distribution is made by overlaying 100 events in order to make the Cherenkov rings more visible. Note that in this overlay, we assume a quantum efficiency (QE) of one for the photodetectors.

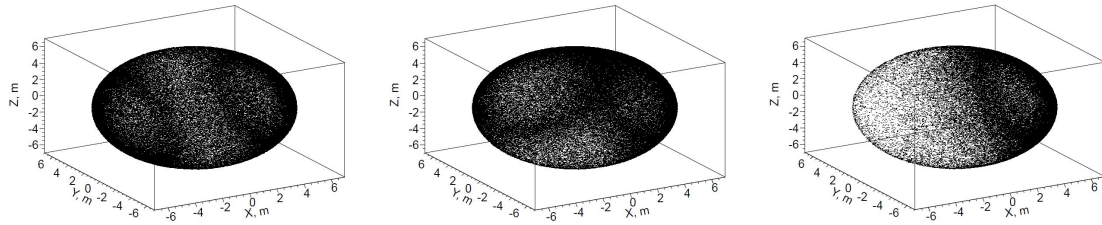


Figure 5: Cherenkov photons distributions on the detector sphere for the three representative event topologies: two back-to-back electrons (*left*), two electrons at  $90^\circ$  angle (*middle*), and a single electron (*center*). All electrons are 5 MeV and originate at the center of the detector. 100 events overlayed for better visibility of the Cherenkov rings. 100% QE is assumed. **These can not be included as PDFs, but my conversion shrunk the size.**

In practice, Cherenkov rings from low energy electrons are not clearly visible. Examples of such Cherenkov clusters, produced by events with a total kinetic energy of 2.539 MeV (the Q-value of  ${}^{130}\text{Te}$ ), are shown in Fig. 6. One can try to guess the event topology by comparing different segments of the detector sphere.

More realistic examples of  ${}^{130}\text{Te}$   $0\nu\beta\beta$ -decay and  ${}^8B$  events simulated at the center of the detector are shown in Fig. 7. Early photoelectrons (PEs), defined as those PEs from Cherenkov and scintillation light within 33.5 ns of the

<sup>1</sup>Only one Cherenkov cluster is produced when either the angle between the two  $0\nu\beta\beta$ -decay electrons is too small or when the energy splits between the electrons in such a way that one electron falls below the Cherenkov threshold.

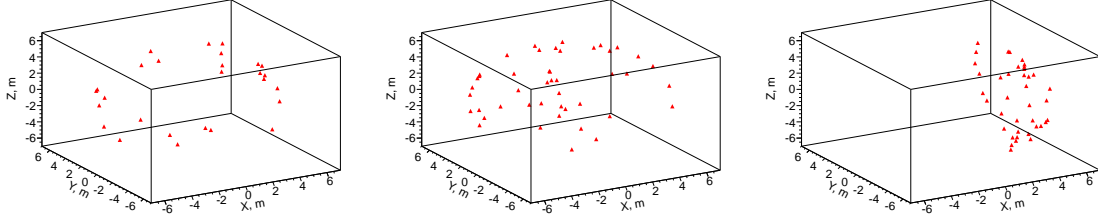


Figure 6: Cherenkov photons distributions on the detector sphere for the three representative event topologies: two back-to-back 1.26 MeV electrons (*left*), two 1.26 MeV electrons at 90° angle (*middle*), and a single 2.529 MeV electron (*center*). All electrons originate at the center of the detector. One randomly selected event is chosen for each category. Default QE is applied.

start of the event, are shown. In this example, the default QE is applied. In this more realistic example, the uniformly distributed scintillation light makes it more difficult to visually distinguish the event topology. Nevertheless, we show that there is still a sufficient difference in the spatial distribution of the early PEs to separate two-track and single-track events using an analysis of spherical harmonics.

### 3.2. Description of Spherical Harmonics Analysis

The central strategy of the analysis is to construct rotationally invariant variables that can be used to separate signal and background events. To this end, let the function  $f(\theta, \phi)$  represent the PE distribution on the detector surface. The function  $f(\theta, \phi)$  can be decomposed into a sum of spherical harmonics:

$$f(\theta, \phi) = \sum_{l=0}^{\infty} \sum_{m=-l}^l f_{lm} Y_{lm}(\theta, \phi), \quad (1)$$

where  $Y_{lm}$  are Laplace's spherical harmonics defined in a real-value basis using Legendre polynomials  $P_l$ :

$$Y_{lm} = \begin{cases} \sqrt{2} N_{lm} P_l^m(\cos\theta) \cos m\phi, & \text{if } m > 0 \\ N_{lm} = \sqrt{\frac{(2l+1)}{4\pi} \frac{(l-m)!}{(l+m)!}}, & \text{if } m = 0 \\ \sqrt{2} N_{l|m|} P_l^{|m|}(\cos\theta) \sin |m|\phi, & \text{if } m < 0 \end{cases} \quad (2)$$

where the coefficients  $f_{lm}$  are defined as

$$f_{lm} = \int_0^{2\pi} d\phi \int_0^\pi d\theta \sin\theta f(\theta, \phi) Y_{lm}(\theta, \phi). \quad (3)$$

Equation 4 defines the power spectrum of  $f(\theta, \phi)$  in the spherical harmonics representation,  $s_l$ , where  $l$  is a multiple moment. The power spectrum,  $s_l$ , is invariant under rotation. It is unique to each of the functions  $f_i(\theta, \phi)$ ,  $i = 1, 2, 3, \dots$ , which can not be transformed into each other by rotation.

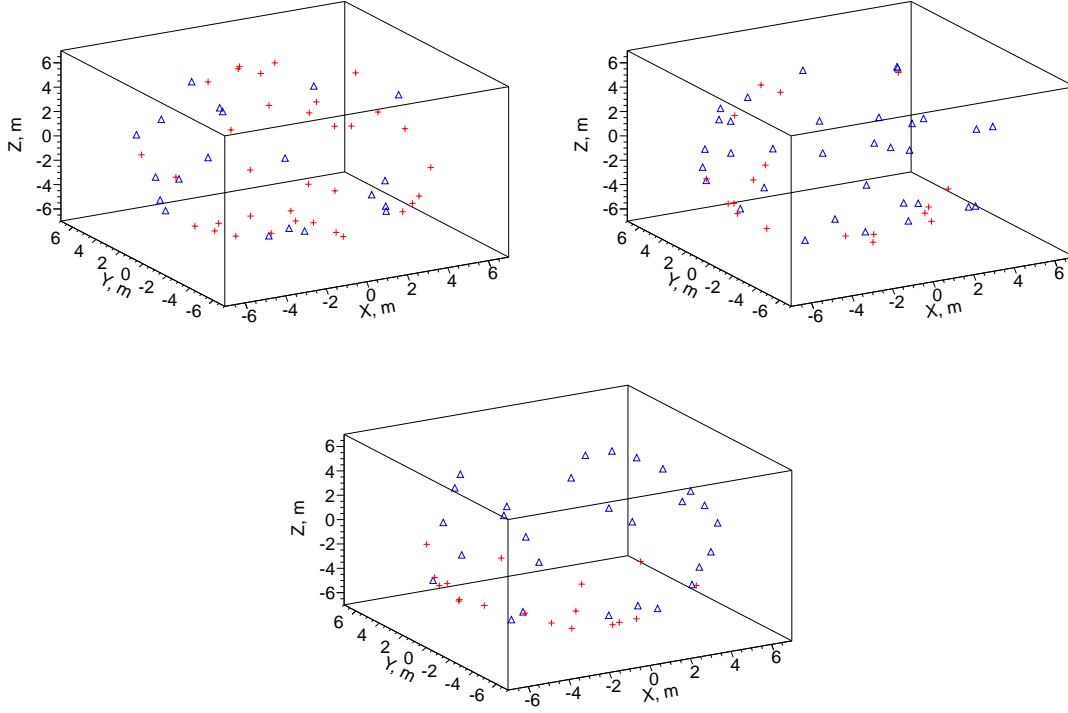


Figure 7: Examples of PEs position on the detector sphere after time cut of 33.5ns. PEs from Cherenkov (red) and scintillation light (blue) are compared. *Top left*:  $^{130}\text{Te}$   $0\nu\beta\beta$  decay back-to-back electrons:  $E_1=1.257$  MeV,  $E_2=1.270$  MeV,  $\cos(\theta)=-0.908$ . *Top right*:  $^{130}\text{Te}$   $0\nu\beta\beta$  decay electrons at  $\sim 90^\circ$ :  $E_1=1.264$  MeV,  $E_2=1.263$  MeV,  $\cos(\theta)=-0.029$ . *Bottom left*:  $^{130}\text{Te}$   $0\nu\beta\beta$  decay electrons at  $\sim 0^\circ$ :  $E_1=1.186$  MeV,  $E_2=1.340$  MeV,  $\cos(\theta)=0.888$ . *Bottom right*: 2.529 MeV single electron. Events are simulated at the center of the detector. Default QE is applied.

$$s_l = \sum_{m=-l}^{m=l} |f_{lm}|^2 \quad (4)$$

The topology of  $0\nu\beta\beta$ -decay signal or background in a spherical detector determines the distribution of the PE's on the detector sphere, and, therefore, a set of  $s_l$ 's. These values can serve as a quantitative figure of merit for different event topologies. The rotation invariance of  $s_l$ 's ensures that this figure of merit does not depend on the orientation of the event with respect to the chosen coordinate frame.

Sum of  $s_l$ 's over all multiple moments equals to the L2 norm of the function  $f(\theta, \phi)$ :

$$\sum_{l=0}^{\infty} s_l = \int_{\Omega} |f(\theta, \phi)|^2 d\Omega. \quad (5)$$

Therefore, the normalized power spectrum,

$$S_l = \frac{s_l}{\sum_{l=0}^{\infty} s_l} = \frac{s_l}{\int_{\Omega} |f(\theta, \phi)|^2 d\Omega}, \quad (6)$$

can be used to compare shapes of various functions  $f(\theta, \phi)$  with different normalization. The total number of PEs detected on the detector sphere fluctuates from event to event, therefore, in all of the following we use the normalized power  $S_l$ .

Figure 8 compares the normalized power spectra for the three representative event topologies that were previously shown in Fig. 5. We note that most of the information is contained in the power spectrum with  $l < 6$ . In most cases we found that there is no need to calculate  $S_l$  for  $l > 3$  to achieve maximal separation between  $0\nu\beta\beta$ -decay and  $^8B$  events. This limit is due to fluctuations in the PE distribution that produce a lot of noise in the power spectrum for higher orders of multiple moments.

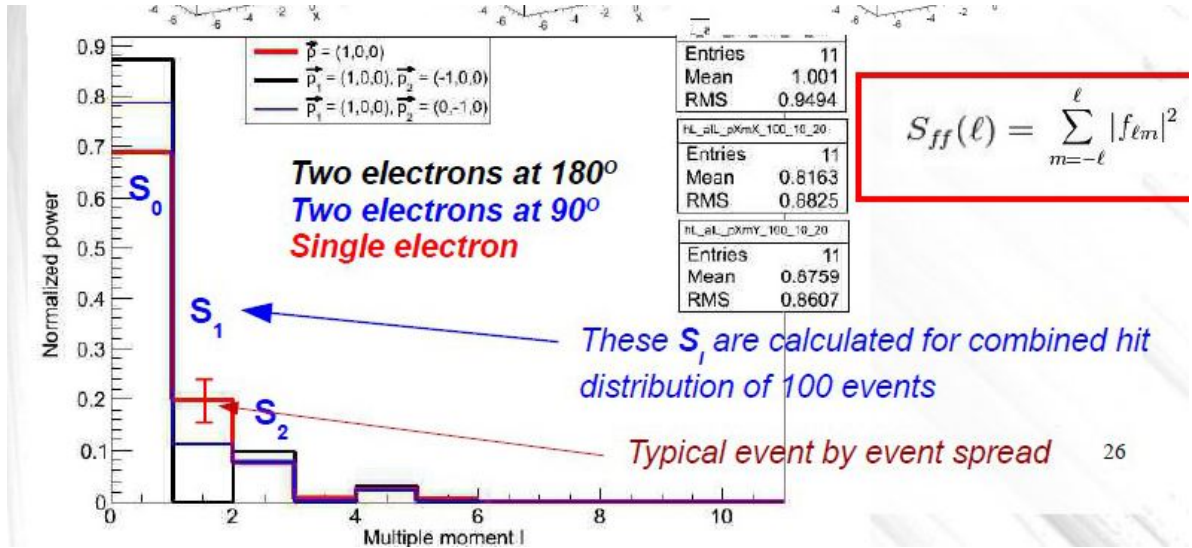


Figure 8: Average  $S_l$  values for two electrons at 180 degree (color1) and 90 degree (color2) 1.5 MeV each and a single electron (color3) with the energy of 3 MeV. Error bars are RMS values of each corresponding individual  $S_l$  distribution (each consists of 1000 events simulated at the center of the detector) indicating typical event-by-event variation.

As shown in the bottom part of Fig. 7,  $0\nu\beta\beta$ -decay events become indistinguishable from single-track events when the angle between the two electrons is small (i.e. they form two overlapping tracks). Event topologies of  $0\nu\beta\beta$ -decay and  $^8B$  events are also very similar when only one electron from  $0\nu\beta\beta$ -decay is above the Cherenkov threshold. Therefore spherical harmonics analysis is most efficient for events with large angular separation between the two electrons and when both electrons are above Cherenkov threshold.

Being able to distinguish between two-tracks and single-track events using the spherical analyses can allow further cuts to be made. For example, one might use absolute directional information to suppress single track events where the direction of the track is consistent with the location of a known background such as the sun. Once a single track topology is established, one can use a centroid method (see Ref. [? ]) to reconstruct directionality of the track (or two

degenerate tracks) in order to suppress events that are aligned with the direction of  $^8B$  solar neutrinos.

### 3.3. Spherical Harmonics Analysis and Off-center Events

The calculation of the normalized power spectrum,  $S_I$ , above, assumes that the coordinate system is located at the location of the interaction. Therefore, in order to compare spherical harmonics for events with vertices not at the center of the detector volume, a coordinate transformation for each photon hit is needed. The necessary transformation applied for each PE within an event is illustrated in Fig. 9. The solid circle in the Figure has a radius,  $R$ , and shows the actual detector boundaries. The dotted circle shows a new sphere with the same radius  $R$ , which now has the event vertex in its center. The radius vector of each PE is stretched or shortened to its intersection with this new sphere using the transformation,  $\vec{r}'_{PE} = \frac{\vec{d}}{|\vec{d}|} \cdot R$ , where  $\vec{r}'_{PE}$  is a new radius vector of a PE and  $\vec{d} = \vec{r}_{PE} - \vec{r}_{vtx}$  with  $\vec{r}_{PE}$  and  $\vec{r}_{vtx}$  being radius vectors of the PE and the vertex in the original coordinates, respectively.

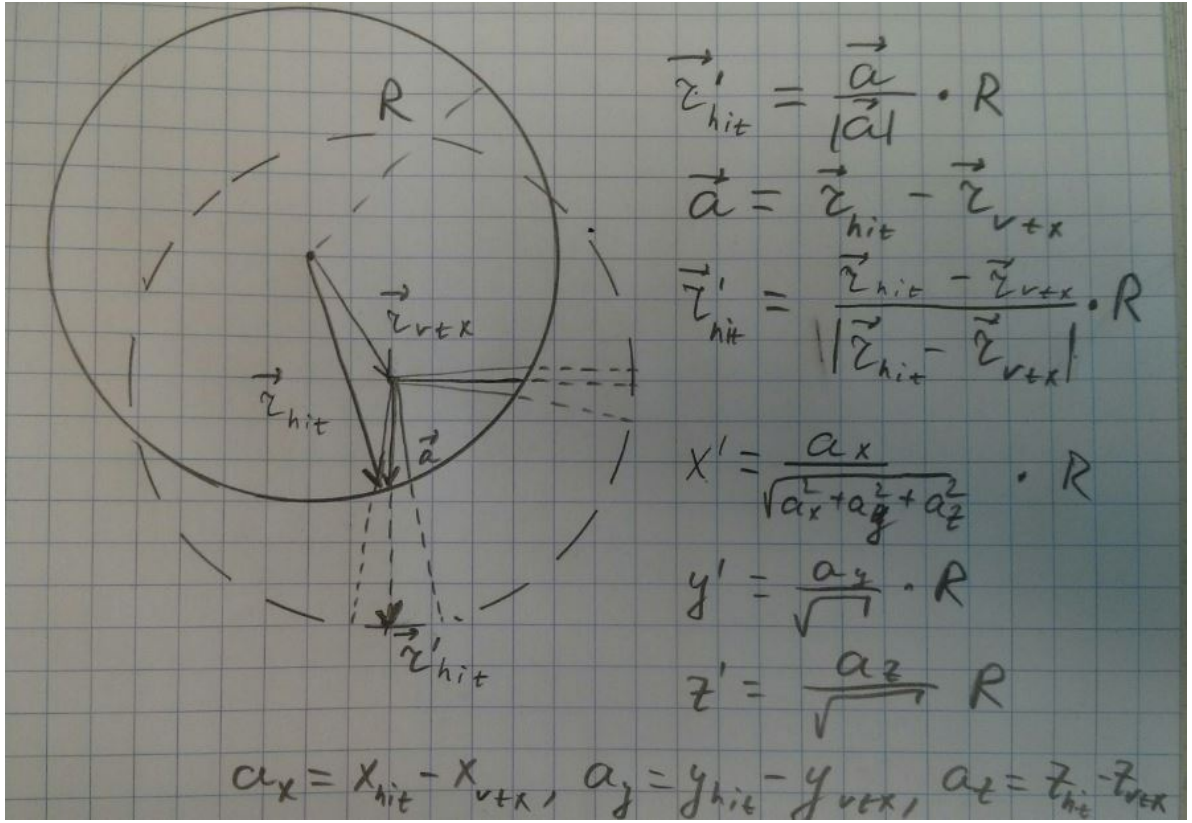


Figure 9: Coordinate transformation applied to events that are off-center. Solid circle schematically shows actual detector boundaries. Dotted circle shows a new sphere of radius  $R=6.5$  m with the event vertex position in the center. The radius vector of each photon hit is stretched or shortened until intersection with this new sphere using transformation  $\vec{r}'_{hit} = \frac{\vec{d}}{|\vec{d}|} \cdot R$ . Where  $\vec{r}'_{hit}$  is a new radius vector of the photon hit,  $R$  is detector sphere radius, and  $\vec{d} = \vec{r}_{hit} - \vec{r}_{vtx}$  with  $\vec{r}_{hit}$  and  $\vec{r}_{vtx}$  being radius vectors of the photon hit and vertex position in original coordinates and correspondingly.

### 3.4. Implementation of the spherical harmonics analysis

For each event, we create a 2-D histogram,  $\theta$  vs  $\phi$ , with the distribution of PEs on the detector surface. We then treat this histogram as a function  $f(\theta, \phi)$  where the value of the function for any pair of  $\theta$  and  $\phi$  is equal to the number

215 of PE in the histogram bin corresponding to that pair.

216 Coefficients  $f_{lm}$  from Eq. 3 are calculated using a Monte Carlo integration technique. Variables  $S_0$ ,  $S_1$ ,  $S_2$ , and  $S_3$   
217 are calculated using Eqs.4 - 6.

218 To illustrate spherical harmonics analysis technique we compare distributions of  $S_0$ ,  $S_1$ ,  $S_2$ , and  $S_3$  for the three  
219 representative event topologies described in Sec. 3.1. Almost all the information about event topology is carried by  
220 Cherenkov light. Therefore we first show spherical harmonics for back-to-back,  $90^\circ$  and single track topologies based  
221 on Cherenkov PEs only (see Fig. 10).

222 Two top panels of Fig. 10 show 2-dimensional distributions,  $S_0$  vs  $S_1$  and  $S_2$  vs  $S_3$ , to demonstrate that all four  
223  $S_l$ 's provide separation between event topologies. No QE is applied in simulation of these events. We also introduce  
224 a 1-dimensional variable,  $S_{01}$  (bottom panel of Fig. 10), that has the best separation power for majority of event  
225 topologies considered in this paper.  $S_{01}$  is defined as a projection of  $S_1$  vs  $S_2$  distribution onto a linear fit of this 2-D  
226 distribution.

227 The effects due to the presence of scintillation light and applying the default QE are shown in Fig. 11. Spherical  
228 harmonics of the same three representative event topologies are now calculated using early light (photons with arrival  
229 time less than 33.5 ns) that contains both directional Cherenkov light and uniform scintillation light. The of number  
230 PE seen by each tube is reduced by the default QE. In this more realistic scenario, the higher order multiple moments,  
231  $S_2$  and  $S_3$ , no longer provide noticeable separation between different event topologies.

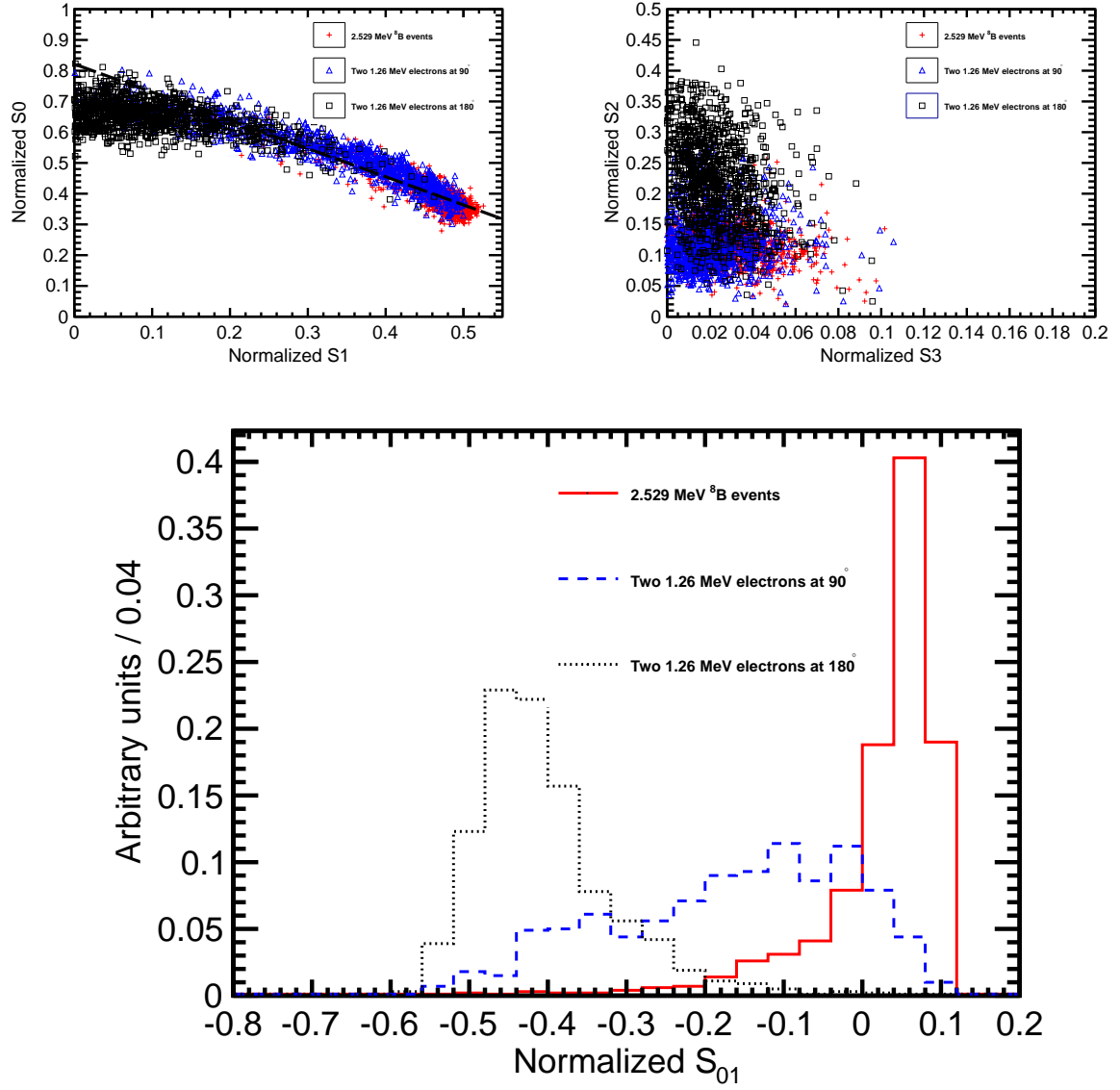


Figure 10: Spherical harmonics for three event topologies: two back-to-back 1.26 MeV electrons (black squares and black dotted line), two 1.26 MeV electrons at  $90^\circ$  angle (blue triangles and blue dashed line), and a single 2.529 MeV electron representing  $^8\text{B}$  background (red crosses and red solid line). Simulation of 1000 events originated at the center of the sphere. Perfect separation between Cherenkov and scintillation light is implemented in this simulation by using only Cherenkov photons. *Top left:*  $S_0$  versus  $S_1$  scatter plot. Black dotted line is a linear fit of the  $90^\circ$  topology and  $^8\text{B}$  events. Variable  $S_{01}$  is defined as a projection of 2D distribution onto this linear fit. *Top right:*  $S_2$  versus  $S_3$  scatter plot. *Bottom:*  $S_{01}$  distributions for the three topologies. These distributions are normalized to unit area for shape comparison.

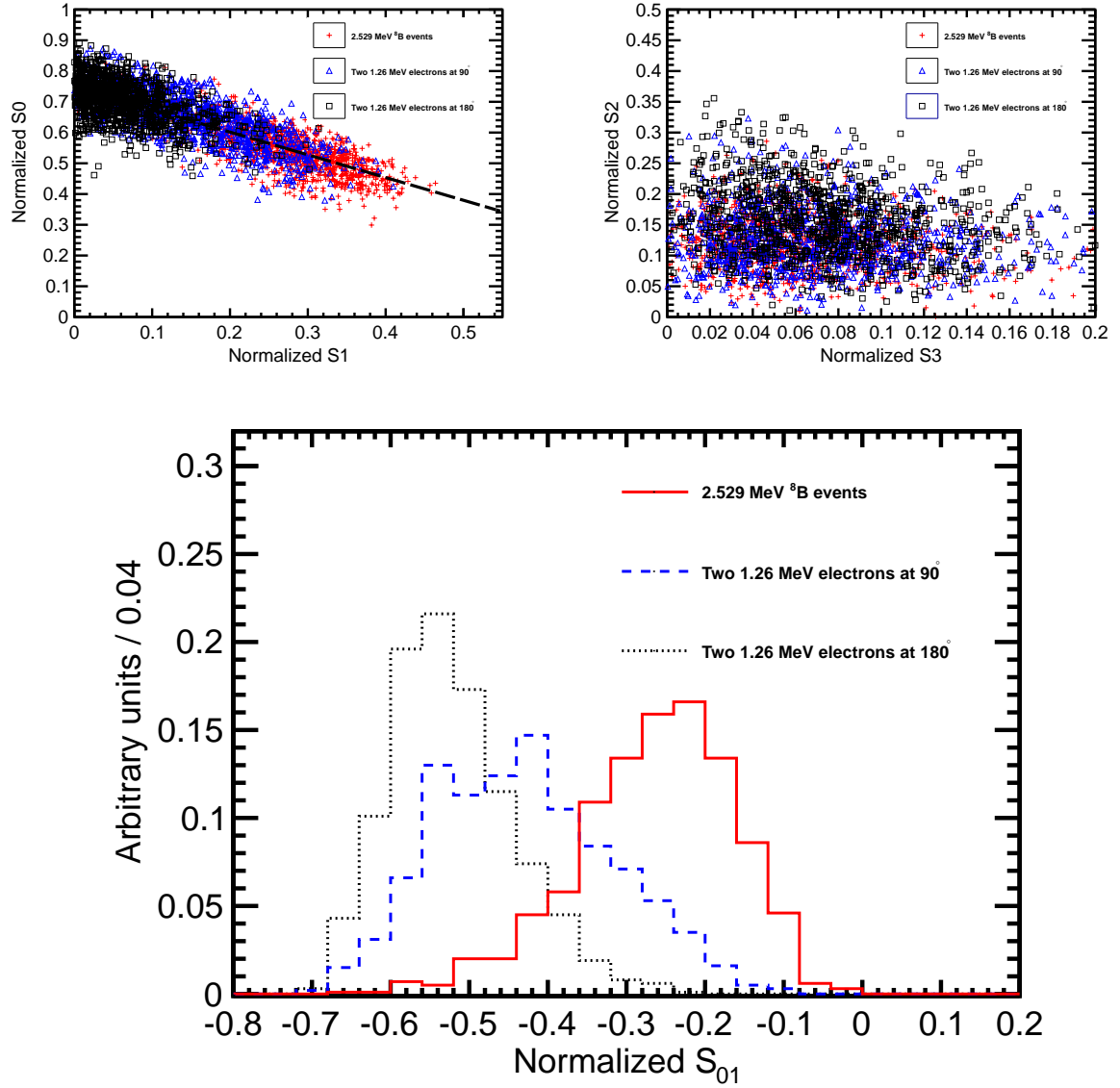


Figure 11: Spherical harmonics for three event topologies: two back-to-back 1.26 MeV electrons (*black squares and black dotted line*), two 1.26 MeV electrons at 90° angle (*blue triangles and blue dashed line*), and a single 2.529 MeV electron representing  $^8\text{B}$  background (*red crosses and red solid line*). Simulation of 1000 events originated at the center of the sphere. Separation between Cherenkov and scintillation light is implemented 33.5 ns cut on the photon arrival time. Perfect vertex reconstruction - true vertex position is used. *Top left*:  $S_0$  versus  $S_1$  scatter plot. Black dotted line is a linear fit of the 90° topology and  $^8\text{B}$  events. Variable  $S_{01}$  is defined as a projection of 2D distribution onto this linear fit. *Top right*:  $S_2$  versus  $S_3$  scatter plot. *Bottom*:  $S_{01}$  distributions for the three topologies. These distributions are normalized to unit area for shape comparison



## 4. Performance and Experimental Challenges

### 4.1. Performance of the spherical harmonics analysis on $0\nu\beta\beta$ decay and ${}^8\text{B}$ events.

Comparison of  $S_0$  and  $S_1$  distributions between  $0\nu\beta\beta$  decay and  ${}^8\text{B}$  events is shown in Fig. 12. There is a noticeable separation between the signal and background. We also note that in the energy range of interest, the  $S_l$ 's do not strongly depend on the energy deposited in the detector, which makes them reliable discriminators at the end point of the  $0\nu\beta\beta$  decay energy spectrum. This makes the information about the event topology complimentary to the energy measurements.

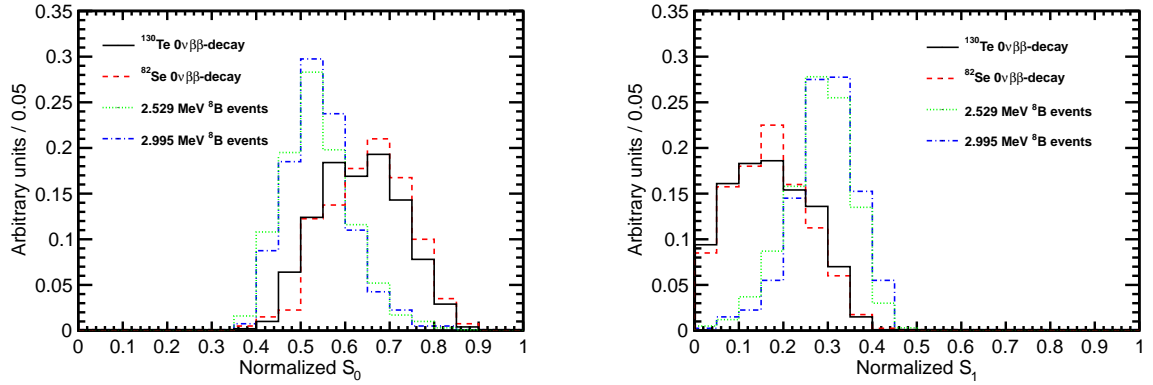


Figure 12:  $S_0$  (left) and  $S_1$  (right) distributions for events with two different event topologies and total kinetic energy.  ${}^{130}\text{Te}$ ,  ${}^{82}\text{Se}$   $0\nu\beta\beta$  decay, 2.529 MeV and 2.995 MeV events are compared. The simulation is done for events with the vertex in the center of the detector.  ${}^8\text{B}$  events are implemented as 2.529 MeV or 2.995 MeV electrons with initial direction along  $x$ -axis. Perfect vertex reconstruction - true vertex position is used. Time cut of 33.5 ns on the photon arrival time is applied.

Figure 13 shows separation between  ${}^{130}\text{Te}$  signal and  ${}^8\text{B}$  background events simulated at the center of the detector. True values of the vertex position and time are used. Also, a time cut of 33.5 ns on the photon arrival time is applied to separate Cherenkov and scintillation light. Most of the discrimination between signal and background comes from  $S_0$  and  $S_1$ . In the following,  $S_2$  and  $S_3$  are not used to separate  ${}^{130}\text{Te}$  and  ${}^8\text{B}$  events (though  $S_2$  and  $S_3$  are helpful for separation of  ${}^{130}\text{Te}$  signal from  ${}^{10}\text{C}$  background. See Appendix.). The scatter plot of  $S_2$  vs  $S_3$  is shown here for completeness.

In order to optimize the separation between  ${}^{130}\text{Te}$  signal and  ${}^8\text{B}$  background, a linear combination of  $S_0$  and  $S_1$ ,  $S_{01}$ , is used. A linear fit,  $S_0 = A \times S_1 + B$ , of the 2-dimensional  $S_0$  vs  $S_1$  scatter plot is performed as shown in Fig. 13. This 2-dimensional distribution then is projected onto the fitted line. **A little bit of math here to quantitatively describe  $S_{01}$  via  $S_0$  and  $S_1$ :** A new coordinate frame is obtained by rotating the original  $S_0$ - $S_1$  frame with the angle  $\theta$  obtained from the fit:  $\tan(\theta)=A$ . A transformation,  $S_{01} = S_1 \cdot \cos(\theta) + S_0 \cdot \sin(\theta)$ , defines the  $S_{01}$  variable. The bottom plot in Fig. 13 shows the performance of  $S_{01}$  to separate  ${}^{130}\text{Te}$  signal and  ${}^8\text{B}$  background events. A fit to this distribution can be done to optimize the discrimination power for a particular experimental setting.

We refrain from quantitative estimates on the improvements in sensitivity to  $0\nu\beta\beta$  decay searches using this method of spherical harmonics as a reliable estimate would require a dedicated analysis taking into account all the details of

a particular experiment.

#### 4.2. Experimental challenges

So far only events at the center of the detector have been considered. In this section we discuss performance of the spherical harmonics analysis for events distributed within the fiducial volume of the detector taking into account finite resolution on vertex position reconstruction.

The absolute cut (e.g., 33.5 ns) on the photon arrival time for central events relies on the fact that, within the uncertainty on electron track length, all photons travel for the same distance before reaching the surface of the detector. PEs with early measured time correspond mostly to Cherenkov photons because of the delay in the scintillation process and longer wavelength of the Cherenkov light.

When the vertex is not at the center, a uniform absolute time cut on the photon arrival time is no longer effective in the selection of Cherenkov photons. In the case of an off-center vertex, there could be a situation when even significantly delayed scintillation photons reach the side of the detector that is closer to the vertex much earlier than Cherenkov photons traveling to the opposite side of the detector. Therefore, the time cut has to take into account the total distance traveled to each PMT by each individual photon.

We found that a relative time cut defined as  $\Delta t = t_{measured}^{phot} - t_{predicted}^{phot} < 1$  ns selects photons with a sufficient fraction being Cherenkov photons. However two factors reduce the Cherenkov/scintillation light separation when this relative time cut is applied.

One reduction in the light separation comes from chromatic dispersion. The predicted time,  $t_{predicted}^{phot} = l/v^{phot}$ , depends on the total distance,  $l$ , traveled by the photon and the velocity of the photon,  $v^{phot}$ . Since the wavelength information is not available for a given PE, we must use an average index of refraction of  $n=1.53$  and define the photon velocity as  $v^{phot} = c/n$ . This uncertainty on the photon velocity due to chromatic dispersion reduces the separation between scintillation and Cherenkov light. The other reduction in the light separation comes from the uncertainty in the reconstructed vertex position. This uncertainty leads to an uncertainty in the photon's total distance traveled and ultimately to a reduction in the Cherenkov/scintillation separation power.

When the whole fiducial volume of the detector is considered only the relative time cut can be used. Therefore, the effectiveness of the spherical harmonics analysis in separating of  $0\nu\beta\beta$  decay and  $^8B$  events is reduced. To demonstrate performance of the spherical harmonics analysis in a more realistic experimental settings we define the fiducial volume within our detector as  $R < 3$  m and simulate  $^{130}Te$   $0\nu\beta\beta$  signal and  $^8B$  background events with vertices uniformly distributed within that fiducial volume.

Figure 14 compares the spherical harmonics for the signal and background events within the fiducial volume. Perfect vertex reconstruction is used in order to isolate the effect due to chromatic dispersion. **Don't understand this fragment: (to be compared with central events shown in Fig. 13).** Next generation LS detectors may be able to recover theses losses due to chromatic dispersion by choosing liquid scintillators with a more narrow emission spectrum (e.g. see Ref [? ]).

Imprecise knowledge of the vertex position due to finite resolution is the second factor affecting performance of the spherical harmonics analysis. The vertex resolution not only reduces Cherenkov/scintillation light separation but it also affects the uniformity of the scintillation light distribution in the early PE sample.

Small deviations in vertex reconstruction cause a large effect on the  $S_0$  and  $S_1$  distributions for the single electron event topology. For the vertices shifted along the direction of the electron track the relative time cut  $\Delta t$  reduces the uniformity of the scintillation light distribution. The  $\Delta t$  cut selects more forward emitted photons in the case when the reconstructed vertex is shifted to the direction opposite to the electron momentum. This enhances the forward region populated by Cherenkov photons and causes a more asymmetric photon distribution that moves  $S_1$  to higher values. The opposite occurs for the case where the reconstructed vertex is shifted in the direction along the electron momentum. Here, the time cut selects more backward emitted photons and counter balances the forward region populated by Cherenkov photons leading to a more symmetric photon distribution and smaller values of  $S_1$ .

Figure 15 shows the performance of the spherical harmonics analysis for events after taking into account a 3 cm vertex reconstruction resolution, applied uniformly within the fiducial volume. Since the goal of this paper is to introduce spherical harmonic analysis we do not perform a full vertex reconstruction and only apply smearing to the simulated vertex position using a Gaussian distribution with sigma of 3 cm on  $x$ ,  $y$ , and  $z$  coordinates.

**Solution to this problem would be a better selection criteria of early light. It has to preserve high admixture of the Cherenkov photons, but needs to select scintillation photons in a more uniform manner. Working on it, but may not be simple so I don't want to include it in this paper.**

Good vertex resolution is essential for spherical harmonics analysis. As one can see in Fig. 15, even a 3 cm vertex resolution reduces the discrimination power of the spherical harmonics analysis.

Such strong dependence on the vertex resolution can be addressed by choosing a different liquid scintillator mixture with a more delayed emission of the scintillation light with respect to the Cherenkov light. With a larger delay in the scintillation light, a high fraction of Cherenkov light in the early PE sample selected with relative time cut  $\Delta t$  can be maintained for a given vertex resolution. In addition, if the fraction of scintillation light is small compared to Cherenkov light, the distortions in the uniformity of the scintillation light distribution due to mis-reconstructed vertex do not significantly affect the  $S_0$  and  $S_1$  variables.

Figure ?? shows spherical harmonics analysis for the simulation where the scintillation component is delayed by an additional 0.5ns compared to our default simulation. Events are simulated uniformly within the fiducial volume of the detector. Vertex resolution of 3 cm is assumed. Noticeable separation between  $0\nu\beta\beta$  and  ${}^8B$  events is achieved.

The discrimination power of the spherical harmonics analysis improves with vertex resolution and more delay in the emission of the scintillation light. Moreover the dependence on vertex reconstruction reduces with delay in the scintillation light.

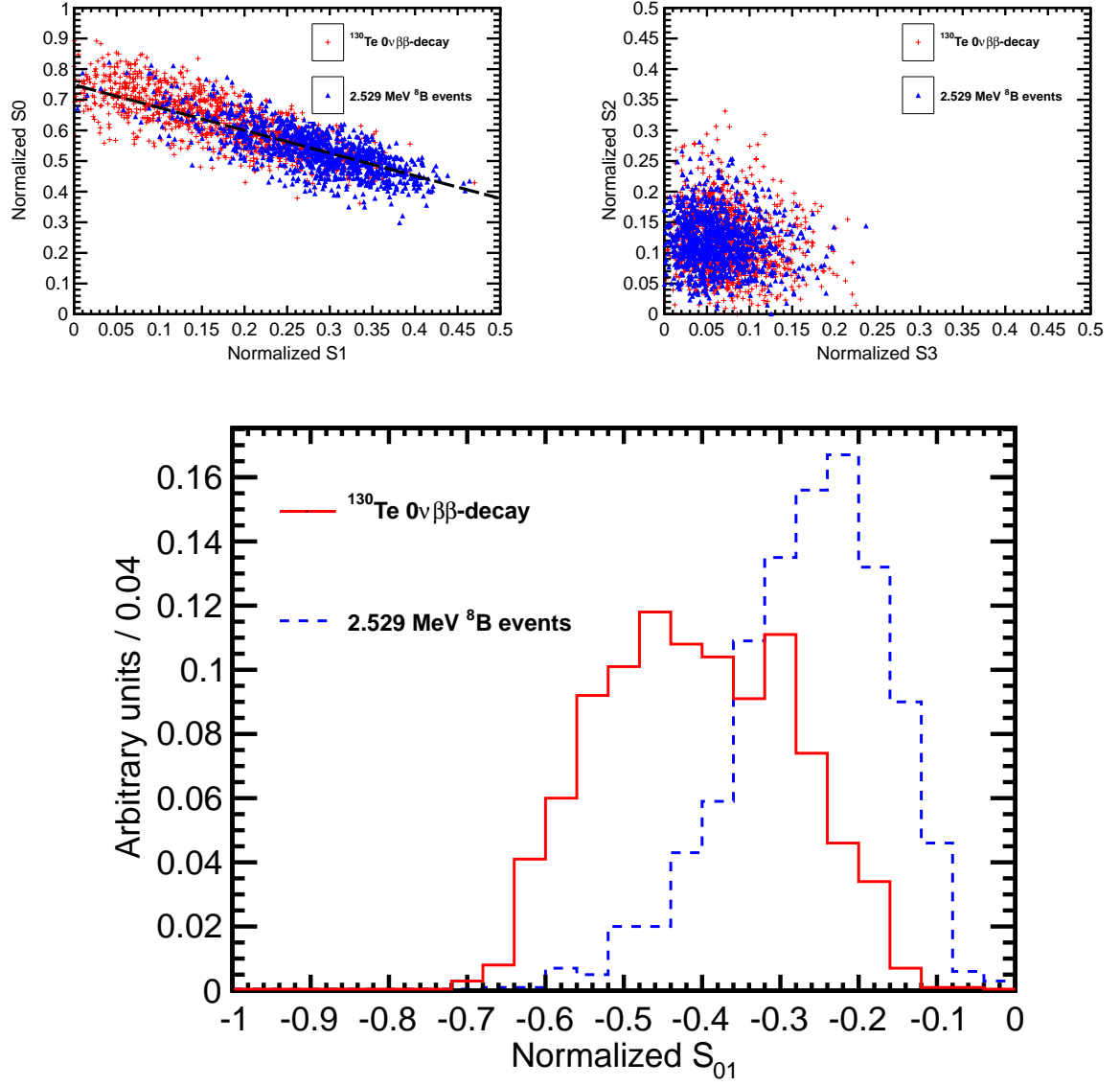


Figure 13: Spherical harmonics comparison between  $^{130}\text{Te } 0\nu\beta\beta$  decay signal ( $Q = 2.529$  MeV) (red) and  $^8\text{B}$  solar neutrinos background (blue) for 1000 simulated events originated at the center of the sphere.  $^8\text{B}$  events are implemented as 2.529 MeV electrons with initial direction along  $x$ -axis. Perfect vertex reconstruction - true vertex position is used. Time cut of 33.5 ns on the photon arrival time is applied. *Top left:*  $S_0$  versus  $S_1$  scatter plot. Black dotted line is a linear fit of these 2D histograms. Variable  $S_{01}$  is defined as a projection of 2D distribution onto this linear fit. *Top right:*  $S_2$  versus  $S_3$  scatter plot. *Bottom:*  $S_{01}$  distribution for the signal and background.

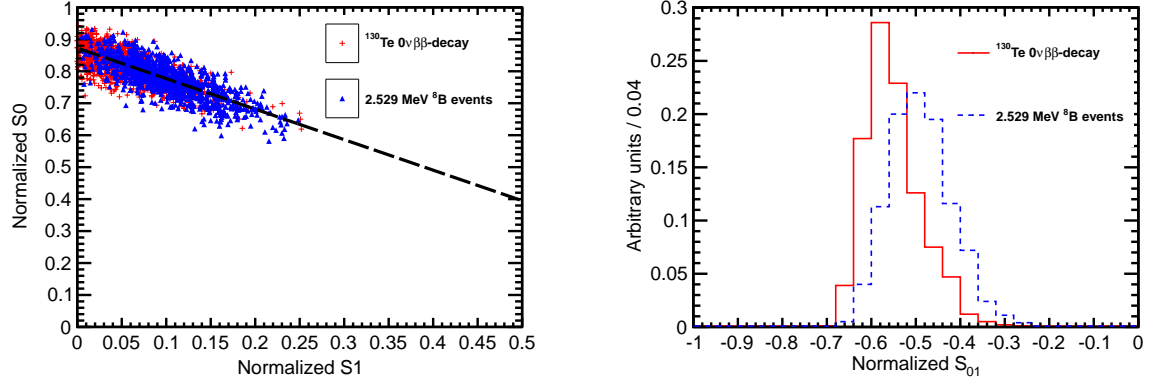


Figure 14: Spherical harmonics comparison between  $^{130}\text{Te}$   $0\nu\beta\beta$  decay signal ( $Q = 2.529$  MeV) (red) and  $^8\text{B}$  solar neutrinos background (blue) for 1000 simulated events. Vertices are uniformly distributed within the fiducial volume,  $R < 3$  m.  $^8\text{Be}$  events are implemented as 2.529 MeV electrons with the initial momentum direction uniformly distributed within  $4\pi$  solid angle. Perfect vertex reconstruction - true vertex position is used. *Left:*  $S_0$  versus  $S_1$  scatter plot. Black dotted line is a linear fit of these 2D histograms. Variable  $S_{01}$  is defined as a projection of 2D distribution onto this linear fit. *Right:*  $S_{01}$

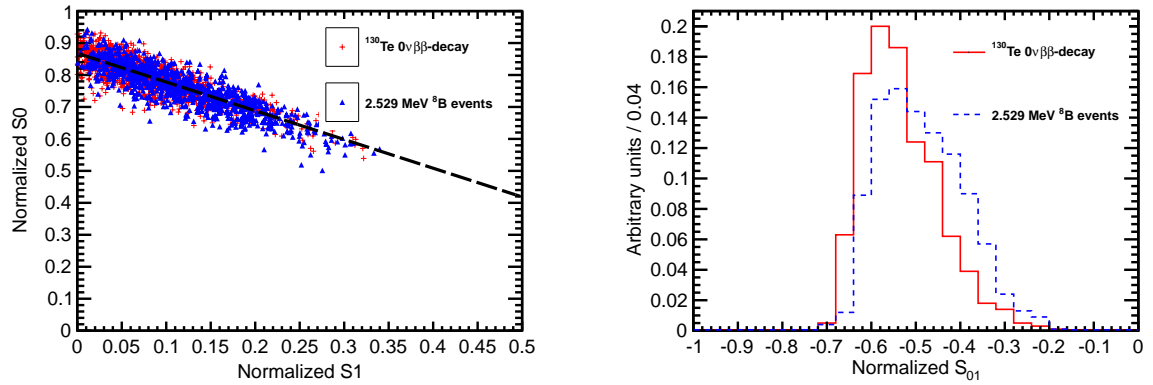


Figure 15: Spherical harmonics comparison between  $^{130}\text{Te}$   $0\nu\beta\beta$  decay signal ( $Q = 2.529$  MeV) (red) and  $^8\text{B}$  solar neutrinos background (blue) for 1000 simulated events. Vertices are uniformly distributed within the fiducial volume,  $R < 3$  m.  $^8\text{Be}$  events are implemented as 2.529 MeV electrons with the initial momentum direction uniformly distributed within  $4\pi$  solid angle. Vertex is smeared with 3 cm resolution. *Left:*  $S_0$  versus  $S_1$  scatter plot. Black dotted line is a linear fit of these 2D histograms. Variable  $S_{01}$  is defined as a projection of 2D distribution onto this linear fit. *Right:*  $S_{01}$

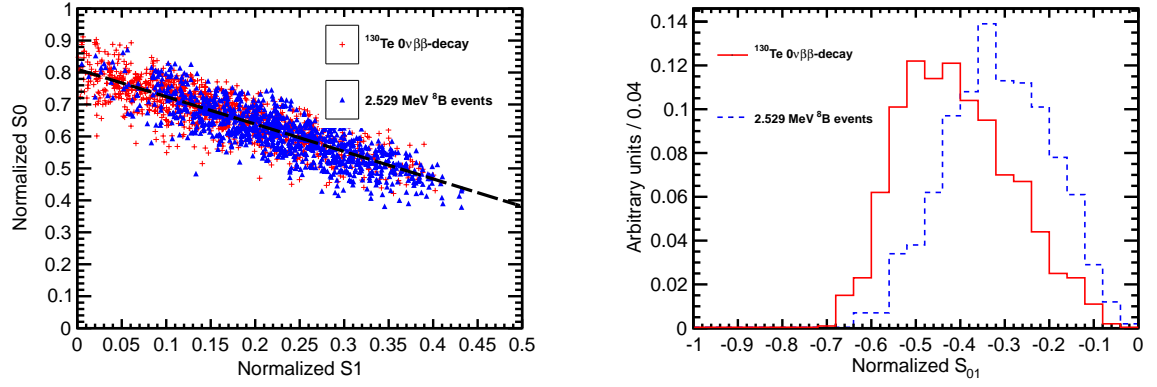


Figure 16: Spherical harmonics comparison between  $^{130}\text{Te } 0\nu\beta\beta$  decay signal ( $Q = 2.529$  MeV) (red) and  $^8\text{B}$  solar neutrinos background (blue) for 1000 simulated events. Vertices are uniformly distributed within the fiducial volume,  $R < 3$  m.  $^8\text{Be}$  events are implemented as 2.529 MeV electrons with the initial momentum direction uniformly distributed within  $4\pi$  solid angle. Vetrex is smeared with 3 cm resolution. **Scintillation light is delayed by additional 0.5 ns.** Left:  $S_0$  versus  $S_1$  scatter plot. Black dotted line is a linear fit of these 2D histograms. Variable  $S_{01}$  is defined as a projection of 2D distribution onto this linear fit. Right:  $S_{01}$

## 5. Conclusions

A technique based on spherical harmonics analysis can separate  $0\nu\beta\beta$  decay from  $^8\text{B}$  solar neutrino interactions. The separation is based on the distinct event topologies of signal and background. This event topology information is available in addition to the measurements of the energy deposited in the detector. This technique may be further developed and adopted by future large scale liquid scintillator detectors to suppress background coming from  $^8\text{B}$  solar neutrino interactions in the detector volume. The performance of the technique is mostly affected by chromatic dispersions, vertex reconstruction and the time profile of the emission of scintillation light. We show that a liquid scintillator detector with a  $\sim 1$  ns total delay of the scintillation light with respect to the Cherenkov light allows for use of the spherical harmonics analysis as an extra handle to extract  $0\nu\beta\beta$  decay signal.

## Acknowledgements

Here are people to acknowledge.

## References

- [1] M. A. Luty, Phys. Rev. D 45 (1992) 455.
- [2] M. Agostini, et al. (GERDA), Phys. Rev. Lett. 111 (2013) 122503.
- [3] K. Alfonso, et al. (CUORE), Phys. Rev. Lett. 115 (2015) 102502.
- [4] J. Albert, et al. (EXO-200), Nature 510 (2014) 229.
- [5] A. Gando, et al. (KamLAND-Zen), Phys. Rev. Lett. 110 (2013) 062502.
- [6] C. Aberle, A. Elagin, H. J. Frisch, M. Wetstein, L. Winslow, J. Instrum. 9 (2014) P06012.
- [7] S. Agostinelli, et al. (GEANT4), GEANT4: A Simulation toolkit, Nucl. Instrum. Meth. A506 (2003) 250–303.
- [8] J. Allison, et al., Geant4 developments and applications, Nuclear Science, IEEE Transactions on 53 (2006) 270–278.
- [9] K. Eguchi, et al. (KamLAND), First results from KamLAND: Evidence for reactor anti-neutrino disappearance, Phys. Rev. Lett. 90 (2003) 021802.
- [10] O. Tajima, *Development of Liquid Scintillator for a Large Size Neutrino Detector*, Master’s thesis, Tohoku University, 2000.
- [11] O. Perevozchikov, *Search for electron antineutrinos from the sun with KamLAND detector*, Ph.D. thesis, University of Tennessee, 2009.
- [12] O. Tajima, *Measurement of Electron Anti-Neutrino Oscillation Parameters with a Large Volume Liquid Scintillator Detector, KamLAND*, Ph.D. thesis, Tohoku University, 2003.
- [13] C. Grant, A Monte Carlo Approach to  $^7\text{Be}$  Solar Neutrino Analysis with KamLAND, Ph.D. thesis, University of Alabama, 2012.
- [14] Hamamatsu Photonics K.K., Large Photocathode Area Photomultiplier Tubes (data sheet, including R7081), 2013. [http://www.hamamatsu.com/resources/pdf/etd/LARGE\\_AREA\\_PMT\\_TPMH1286E05.pdf](http://www.hamamatsu.com/resources/pdf/etd/LARGE_AREA_PMT_TPMH1286E05.pdf).
- [15] Y. Abe, et al. (Double Chooz), Reactor electron antineutrino disappearance in the Double Chooz experiment, Phys. Rev. D86 (2012) 052008.
- [16] Electromagnetic Standard Physics Working Group, 2013. [http://www.geant4.org/geant4/collaboration/working\\_groups/electromagnetic/index.shtml](http://www.geant4.org/geant4/collaboration/working_groups/electromagnetic/index.shtml).
- [17] H. Grabas, R. Obaid, E. Oberla, H. Frisch, J.-F. Genat, R. Northrop, F. Tang, D. McGinnis, B. Adams, M. Wetstein, {RF} strip-line anodes for psec large-area mcp-based photodetectors, Nucl.Instrum.Meth. A 711 (2013) 124 – 131.
- [18] Oberla, E. and Genat, J. and Grabas, H. and Frisch, H. and Nishimura, K. and Varner, G., A 15 GSa/s, 1.5 GHz Bandwidth Waveform Digitizing ASIC, Nucl.Instrum.Meth. A735 (2014) 452–461.
- [19] B. Adams, et al., Invited article: A test-facility for large-area microchannel plate detector assemblies using a pulsed sub-picosecond laser, Review of Scientific Instruments 84 (2013) 061301.
- [20] B. Adams, et al., Measurements of the gain, time resolution, and spatial resolution of a  $20\times 20\text{cm}^2$  MCP-based picosecond photo-detector, Nucl.Instrum.Meth. A732 (2013) 392–396.
- [21] O. Seigmund, et al., Large area event counting detectors with high spatial and temporal resolution, J. Instrum. 9 (2014) C04002.
- [22] B. Adams, et al., An internalALD-basedhighvoltagedividerandsignalcircuit for MCP-basedphotodetectors, Nucl.Instrum.Meth. A780 (2015) 107–113.
- [23] B. Adams, et al., Timing characteristics of Large Area Picosecond Photodetectors, Nucl.Instrum.Meth. A795 (2015) 1–11.
- [24] M. Minot, et al., Pilot production & commercialization of LAPPD<sup>TM</sup>, Nucl.Instrum.Meth. A787 (2015) 78–84.

## A. $0\nu\beta\beta$ decay vs $^{10}\text{C}$ background

Other common backgrounds to  $0\nu\beta\beta$  decay search include radioactive decays of nuclei that are excited by cosmic muons and produced through the decays of Th and U naturally present in the materials. In liquid scintillator detectors, most of events from Th and U decays occur in the materials of the scintillator enclosure. Typically, they enter the fiducial volume as 2.6 MeV gammas. These gammas pass into the fiducial volume either because they showered too late or have mis-reconstructed vertex. Both effects depend on details of a particular experiment and in this paper we make no attempt to introduce a topology reconstruction for the backgrounds coming from Th and U lines. Cosmic induced backgrounds, to the contrary, are more generic and originate inside the fiducial volume. In this section we discuss event topology of  $^{10}\text{C}$  events that are most relevant in the energy of 2-3 MeV.

Typical energy deposition by  $^{10}\text{C}$  events is shown in Fig. A.17. We propose to use spherical harmonics analysis to separate  $0\nu\beta\beta$  decay events from  $^{10}\text{C}$  events that within energy resolution overlap with the  $0\nu\beta\beta$  decay Q-value.



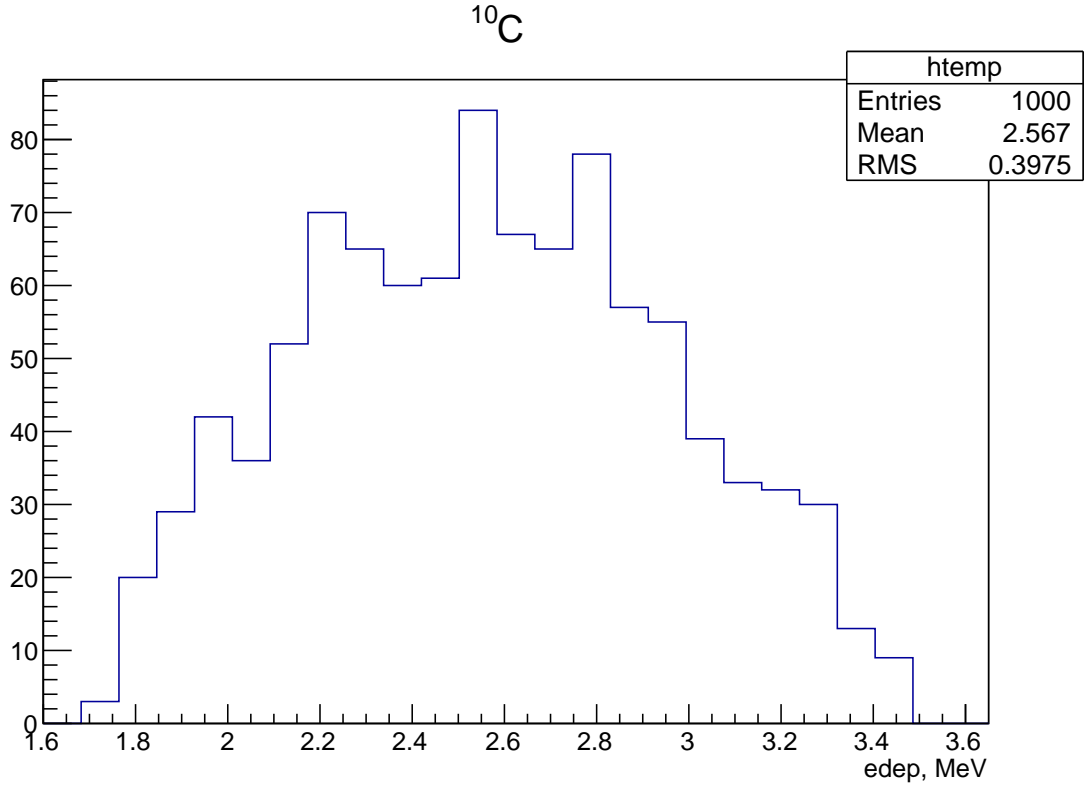


Figure A.17: Energy deposition in  $^{10}\text{C}$  events.

375 We note that 98% of  $^{10}\text{C}$  decays through the excited state of  $^{10}\text{B}(718)$ , which has a half-life time of  $\sim 1$  ns.  
 376 Therefore, the majority of  $^{10}\text{C}$  events have a prompt positron accompanied by a delayed 0.718 MeV gamma. This  
 377 delayed gamma affects the PE arrival time distribution. Figure A.18 compares the shape of the PE arrival time  
 378 distribution between  $^{130}\text{Te}$   $0\nu\beta\beta$  decays and  $^{10}\text{C}$  events. The time profile of the scintillation photons can be used to  
 379 separate signal from  $^{10}\text{C}$  events.

380 Comparison of spherical harmonics is shown in Fig. A.19.  $^{10}\text{C}$  events are generated at the center of the detector.  
 381 True vertex position is used to apply a 33.5 ns time cut to select photons for the spherical harmonics analysis. The  
 382 separation is seen in S0 vs S1 and S2 vs S3 scatter plots. We project both scatter plots to a line that gives maximum  
 383 separation (two bottom panels in Fig. A.19). There is enough separation between the distributions to suggest that this  
 384 analysis can be used to distinguish between  $0\nu\beta\beta$  and  $^{10}\text{C}$  events.

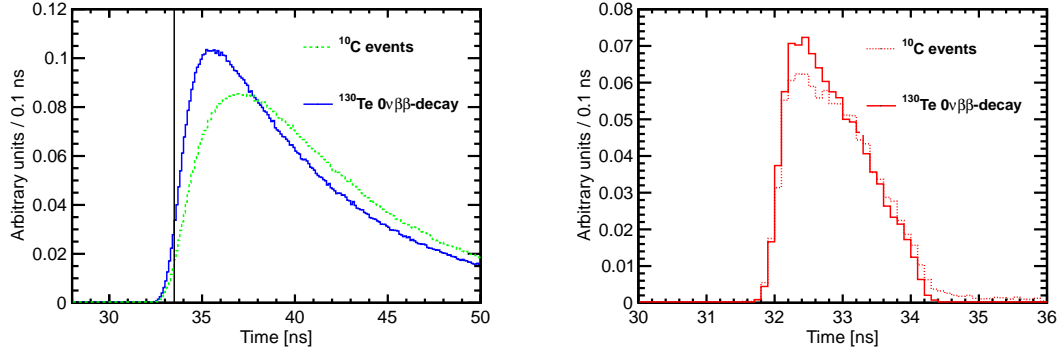


Figure A.18: Photo-electron (PE) arrival times after application of the photo-detector transit time spread (TTS) of 100 ps for the simulation of 1000  $0\nu\beta\beta$  decay events of  $^{130}\text{Te}$  (solid lines) and  $^{10}\text{C}$  (dotted lines) events at the center of the detector. All distributions are normalized for shape comparison. **Absolute number of PEs per event depends on the total energy deposited in the detector. Figure A.17 shows energy deposited in the detector in  $^{10}\text{C}$  events.** *Left:* Scintillation PEs arrival time. The black vertical line illustrates a time cut at 33.5 ns. *Right:* Cherenkov PEs arrival time.

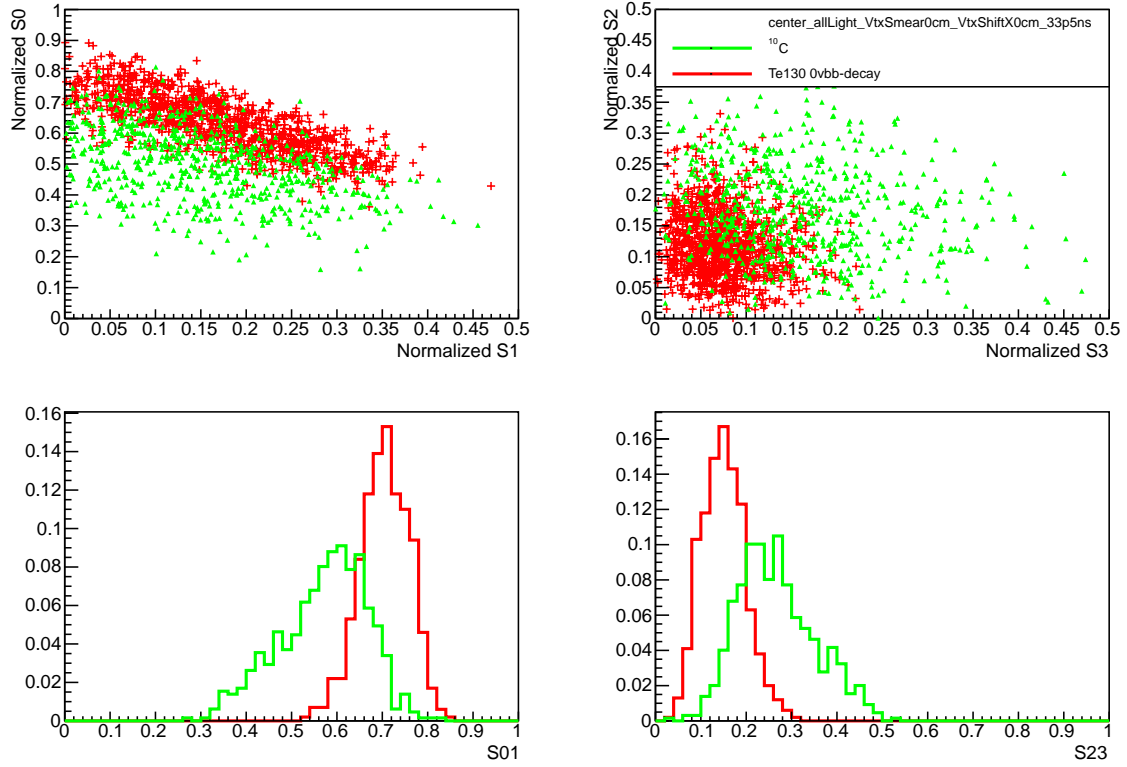


Figure A.19: Spherical harmonics comparison between  $^{130}\text{Te}$   $0\nu\beta\beta$  decay signal ( $Q = 2.529$  MeV) (red) and  $^{10}\text{C}$  solar neutrinos background (blue) for 1000 simulated events originated at the center of the sphere.  $^{10}\text{C}$  with energy deposition between 2.1 MeV and 2.9 MeV are considered. Perfect vertex reconstruction - true vertex position is used. Time cut of 33.5 ns on the photon arrival time is applied. *Top left:*  $S_0$  versus  $S_1$  scatter plot. *Top right:*  $S_2$  versus  $S_3$  scatter plot. *Bottom left:* Distribution of the  $S_{01}^{C10}$  variable calculated for signal (red) and background (green). *Bottom right:* Distribution of the  $S_{23}^{C10}$  variable calculated for signal (red) and background (green).